Boundary-Layer Meteorol (2015) 154:265–289
DOI 10.1007/s10546-014-9973-8

ARTICLE

The Challenge of Forecasting the Onset and Development of Radiation Fog Using Mesoscale Atmospheric Models

G. J. Steeneveld · R. J. Ronda · A. A. M. Holtslag

Received: 14 October 2013 / Accepted: 2 October 2014 / Published online: 25 October 2014

Abstract The numerical weather prediction of radiation fog is challenging, as many models typically show large biases for the timing of the onset and dispersal of the fog, as well as for its depth and liquid water content. To understand the role of physical processes, i.e. turbulence, radiation, land-surface coupling, and microphysics, we evaluate the HARMONIE and Weather Research and Forecasting (WRF) mesoscale models for two contrasting warm fog episodes at the relatively flat terrain around the Cabauw tower facility in the Netherlands. One case involves a radiation fog that arose in calm anticyclonic conditions, and the second is a radiation fog that developed just after a cold front passage. The WRF model represents the radiation fog well, while the HARMONIE model forecasts a stratus lowering fog layer in the first case and hardly any fog in the second case. Permutations of parametrization schemes for boundary-layer mixing, radiation and microphysics, each for two levels of complexity, have been evaluated within the WRF model. It appears that the boundary-layer formulation is critical for forecasting the fog onset, while for fog dispersal the choice of the microphysical scheme is a key element, where a double-moment scheme outperforms any of the single-moment schemes. Finally, the WRF model results appear to be relatively insensitive to horizontal grid spacing, but nesting deteriorates the modelled fog formation. Increasing the domain size leads to a more scattered character of the simulated fog. Model results with one-way or two-way nesting show approximately comparable results.

Keywords Cabauw · Domain size · Grid nesting · HARMONIE model · Mesoscale modelling · Radiation fog · WRF model

1 Introduction

Fog consists of water droplets and/or ice crystals that are suspended close to the Earth's surface, (Brown and Roach 1976) i.e. it is a low-level stratus cloud (Gultepe et al. 2007). Fog

G. J. Steeneveld (✉) · R. J. Ronda · A. A. M. Holtslag
Meteorology and Air Quality Section, Wageningen University, P.O. Box 47,
6700 AA Wageningen, The Netherlands
e-mail: gert-jan.steeneveld@wur.nl

limits the visibility and thus affects human activities that rely on good visibility conditions. These activities are part of the core activities of modern societies, most notably aircraft operations (landing and taxiing to and from the runway), shipping (Fu et al. 2006, 2010), and road traffic (Bartok et al. 2012). Moreover, fog is an important aspect of the climate in certain regions (Syed et al. 2012). Finally, fog influences the health of vulnerable groups, since hospital visits increase during foggy nights (Tanaka et al. 1998).

Fog occurs when relatively warm and moist air is cooled or moistened until the temperature of the air reaches the dewpoint and consequently becomes saturated, provided sufficient condensation nuclei are present. According to the pathways that can lead to the saturation of air, fog is classified into different fog types. A frequently occurring fog type, especially for relatively flat areas such as the Netherlands, is radiation fog, which occurs in clear-sky conditions with relatively low wind speed. In these conditions air close to the surface cools from the evening transition onwards because the absence of clouds leads to strong radiation loss from air close to the Earth's surface (Ha and Mahrt 2003; Savijärvi 2006; Edwards 2009; Steeneveld et al. 2010), while low wind speeds hamper a sufficient supply of sensible and latent heat toward the surface (Duynkerke 1991, 1999).

Despite the major economic impact of radiation fog on human society, numerical weather prediction (NWP) models have relatively low skill in forecasting both the onset and the development of radiation fog (Teixeira 1999; Gultepe et al. 2007; Tudor 2010; Zhou et al. 2011; Román-Cascón et al. 2012). For complex terrain with closed basins, high resolution NWP models provide reasonable results since the problem is confined to the basin, and katabatic flows induce the collection of relatively cold air at the bottom of the basin (Müller et al. 2010; Cuxart and Jiménez 2011). Unfortunately such a confining mechanism is absent over flat terrain, which makes fog forecasting even more challenging. Then, radiation fog is the result of an intricate balance of a myriad of processes that act upon near-surface air. This balance is difficult to achieve in NWP models. For instance, Tudor (2010) showed that the ARPEGE ("Action de Recherche Petite Echelle Grande Echelle") model did not forecast radiation fog for a selected event in Hungary and Croatia in December 2004. For the same fog event the limited-area model "Aire Limitée Adaptation dynamique Développement InterNational" (ALADIN) was only able to reproduce the 2-m air temperature and relative humidity (RH) observations at different SYNOP weather stations after major refinements of the parametrization schemes for radiation, microphysics, horizontal diffusion, and boundary-layer turbulence. Van der Velde et al. (2010) showed that both the High-Resolution Limited Area Model (HIRLAM) model and the Weather Research and Forecasting (WRF) mesoscale model were unable to simulate the onset and development of radiation fog under frost conditions over the Netherlands.

Because three-dimensional (3D) models, even when run with a relatively high resolution, have severe problems in simulating the fog onset and development, both the forecasting of fog and the related research activities rely on detailed, mostly, single-column models (Bergot et al. 2007; Stolaki et al. 2011). Some models have especially been designed for fog research and forecasting, such as the Code de Brouillard à l 'Echelle Locale (COBEL) model developed by Bergot and Guedalia (1994) and Bergot et al. (2005), and the microphysical fog (MIFOG) and parametrized fog (PAFOG) models developed by Bott et al. (1990) and Bott and Trautmann (2002). Though important, a correct description of the physical processes within a single-column model is not always sufficient to forecast the fog onset and development successfully. Many of the cited studies underline the importance of applying a sufficiently high vertical resolution to resolve the major processes, while especially Bergot and Guedalia (1994) and Bergot et al. (2005) found that successful fog forecasting requires an accurate model initialization (e.g. Rémy and Bergot 2009). In many cases the use of local observations

was a prerequisite for a successful initialization, as simulations with a single-column model initialized with the fields from a NWP model failed to forecast the onset of radiation fog.

The aim of the present study is to evaluate the skill of two state-of-the-art atmospheric mesoscale models (WRF and HARMONIE) in forecasting the occurrence and development of fog for two contrasting warm fog episodes in the flat area of the Netherlands. This is more demanding than for complex terrain since the pooling of cold air by topography is absent in flat terrain. The evaluation is performed against micrometeorological observations at Cabauw in the Netherlands (Beljaars and Bosveld 1997). Since both models are used for operational forecasting, such a study is relevant in the understanding of differences in model results, providing guidelines to operational users of these models, and also should facilitate the pinpointing of further model development. As such, we do not aim to rank the models, but identify their strengths and weaknesses, with an outlook to model improvement.

The WRF model offers multiple parametrization options for the representation of boundary-layer turbulence, radiation, and microphysics. We aim to identify which of the schemes and their relative complexities are essential in the forecasting of the fog onset, its vertical development and its dissipation. Many earlier studies were specifically devoted to the role of model vertical resolution. Here we extend these studies by assessing the model results regarding technical aspects such as domain size, spatial resolution and grid nesting. Although the presence of model sensitivity to these aspects is qualitatively known from daily practice, they have hardly been studied systematically (e.g. Kleczek et al. 2014), particularly for fog. Idealized studies by Warner et al. (1997), Leduc and Laprise (2009) and Leduc et al. (2011) found that the development of small-scale atmospheric structures in model simulations was underestimated if the domain size is too small. Therefore, we quantify this model sensitivity in the context of fog forecasting.

Also, grid nesting is often used to obtain enhanced resolution in areas of special interest within the model domain. Nesting is typically performed by interpolating fields in the boundary zone of the nested domain (typically a few grid points), and even after the flow has passed through this boundary zone, a large spin-up region is required for developing small-scale features. Hence nesting may seriously affect the development of small-scale features and fog onset, and this impact is quantified here.

The article is structured as follows: Sect. 2 presents for each fog episode the weather conditions and the spatial extension of the fog within the Netherlands. Section 3 describes the models that have been applied in the skill evaluation, while Sect. 4 is concerned with the observations used to validate the models. Sections 5 and 6 present for each fog episode the results of the models as compared to the observations, and in Sect. 7 results are summarized and conclusions drawn.

2 Synoptic Settings

This section presents the synoptic conditions for the two selected fog episodes under study. We note that operations at Amsterdam Airport were severely hampered during both episodes, for example; fog episode 1 (6 October 2005) led to reduced airport capacity from 68 to 22 planes per hour.

2.1 Fog Episode 1: 5 and 6 October 2005

During the episode of 5–7 October 2005, the synoptic situation over the Netherlands was dominated by a surface anticyclone that progressed in a north-easterly direction from southern

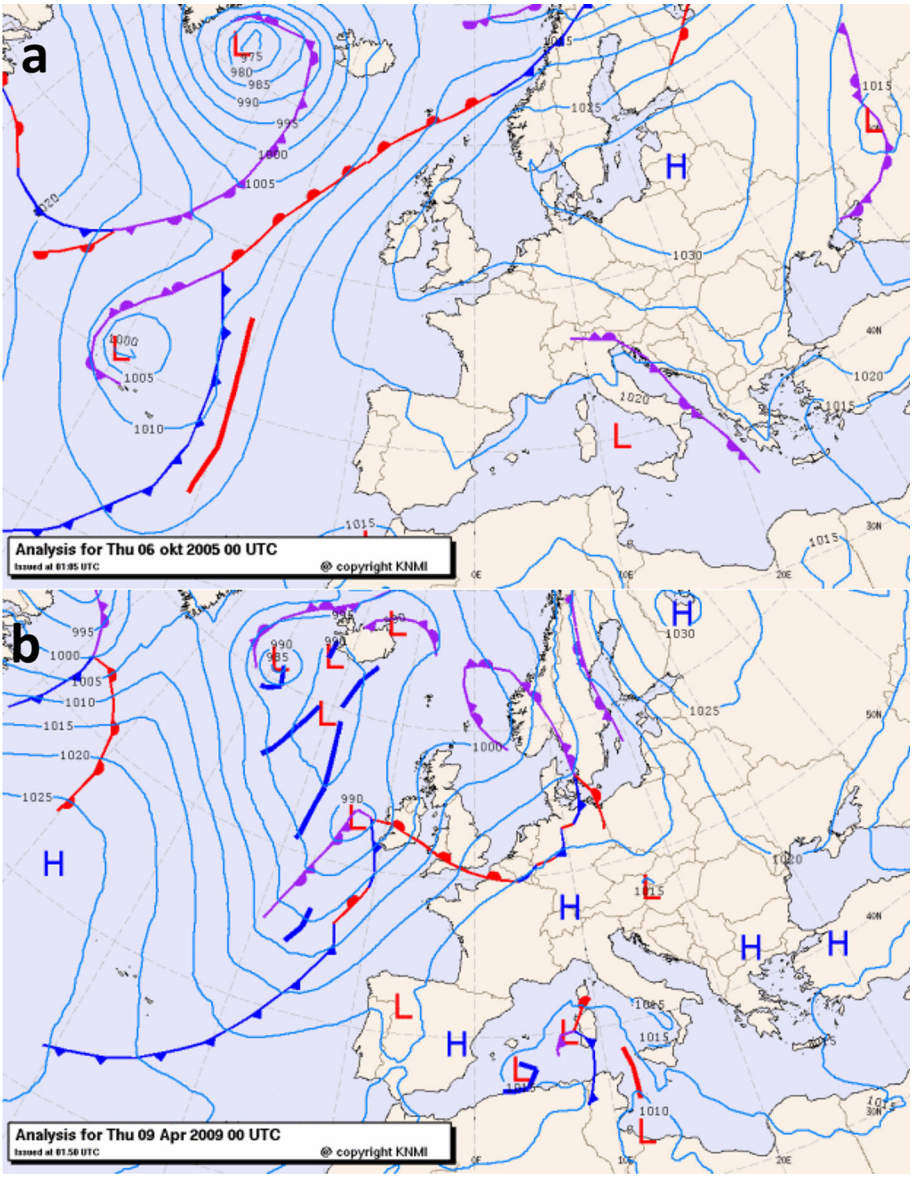

Fig. 1 Operational analysis of the synoptic situation over Europe for 6 October 2005, 0000 UTC (**a**) and 9 April 2009, 0000 UTC (**b**)

Ireland toward western Russia (Fig. 1a). During the night of 5–6 October 2005 the anticyclone was located over the Baltic Sea, generating an easterly flow with low wind speeds over the Netherlands. Mean wind speeds measured at Amsterdam airport reached 4 m s^{-1}.

The weather conditions favoured the formation of radiation fog during the mornings of 5 and 6 October 2005, as illustrated in a series of visibility maps (Fig. 2). On 5 October 2005 at 0000 UTC the visibility over the entire Netherlands was greater than 5 km. On 5 October

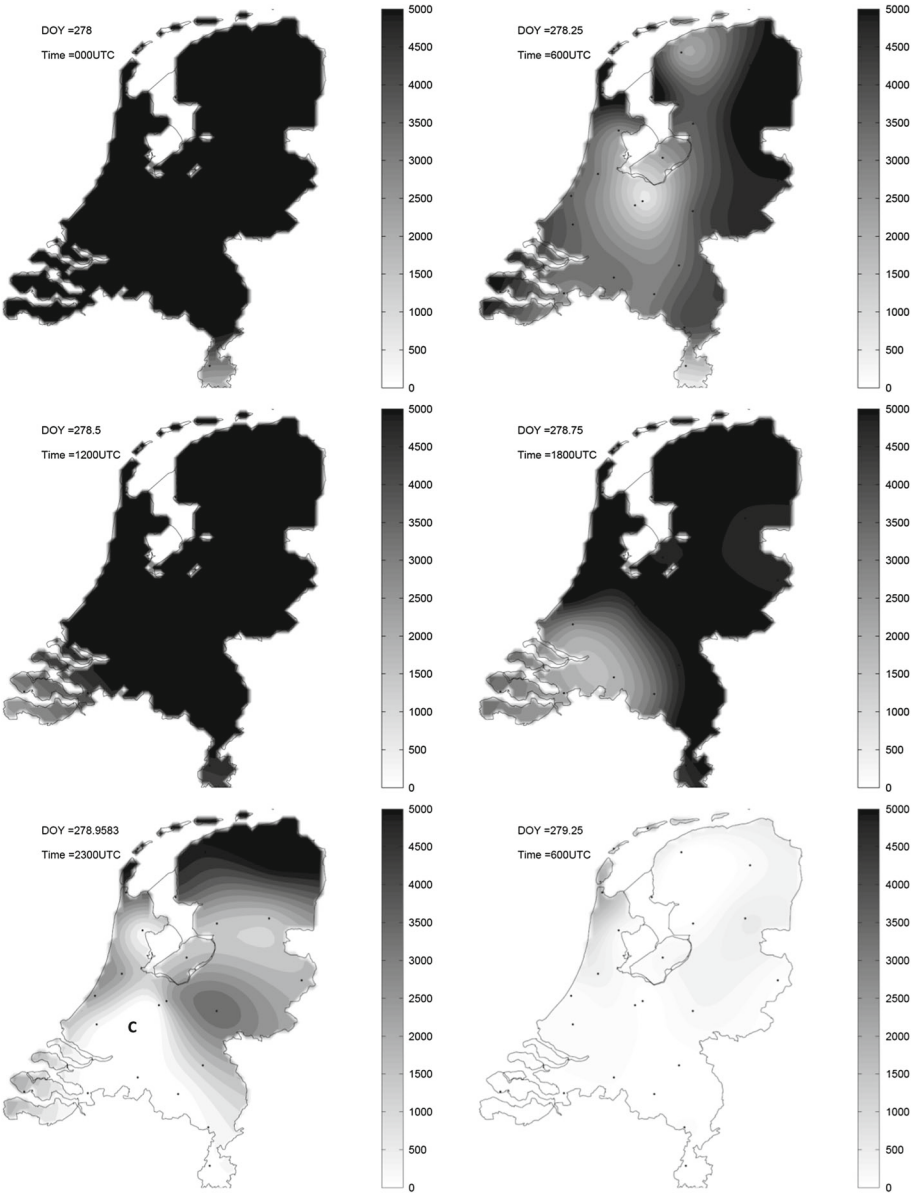

Fig. 2 Observed visibility in the synoptic network over the Netherlands during fog episode 1 (5–6 October 2005). *C* indicates the location of Cabauw

2005 at 0600 UTC, the fog appears in the south-western part of the country, and on 5 October 2005 at 1200 UTC the fog has mostly dissipated and the visibility is again greater than 5 km in most parts of the country. Fog reformed in the south-west on 5 October 2005 at 1800 UTC, and visibility continued to be poor until the morning of 6 October 2005.

Cabauw tower observations indicate that the fog reaches the 200 m level on both nights (Fig. 3a). Also, the vertical temperature structure during the fog event does not show strong

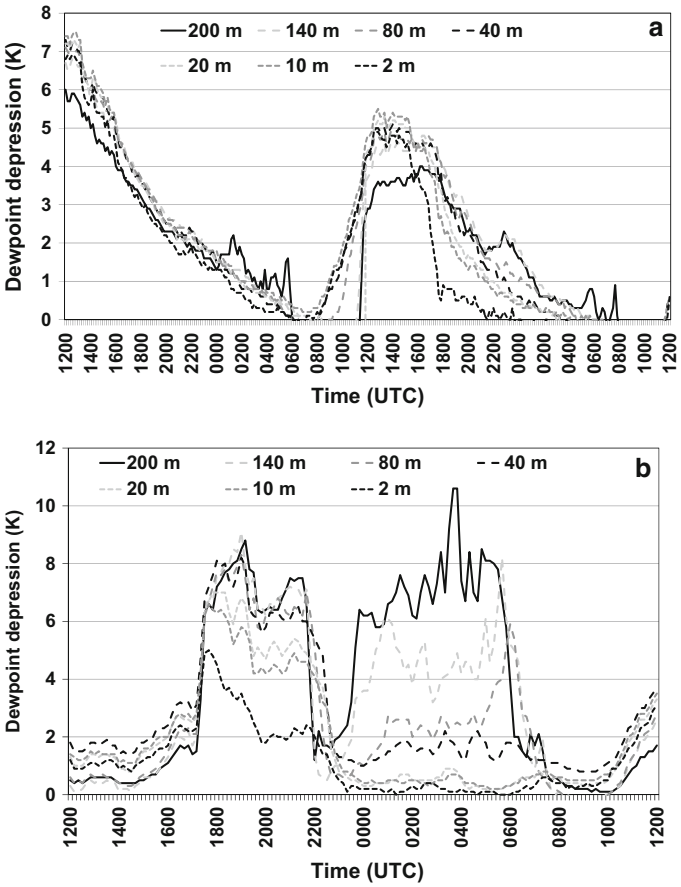

Fig. 3 Observed dewpoint depression at the Cabauw tower facility for the period 4 October 1200 UTC to 6 October 1200 UTC (**a**), and 8 April 2009, 1200 UTC to 9 April 2009, 1200 UTC (**b**)

stratification close to the surface, indicating that the fog is vertically well-developed and mainly driven by radiative cooling at the fog top.

2.2 Fog Episode 2: 8 and 9 April 2009

On 8 and 9 April 2009, the synoptic situation in the Netherlands was dominated by an anticyclone over central Europe and a cyclone close to Ireland (Fig. 1b). On 9 April 2009 at 0000 UTC a warm front was located over northern France, while a cold front was located near the south-eastern portion of the Netherlands. During 9 April 2009 the warm front passed in a north-easterly direction over the country. The weather was characterized by a south-westerly flow with high wind speeds during the daytime on 8 April 2009, and very low wind speeds during the late evening of 8 April 2009 and the early morning of 9 April 2009. The low wind speed and cleared skies after the frontal passage initiated surface cooling, and favoured fog formation in the early morning of 9 April 2009.

The visibility evolution shows that on 8 April 2009 at 1800 UTC, the country is fog free (Fig. 4), while at 2300 UTC fog appears in the eastern part. On 9 April 2009 at 0400

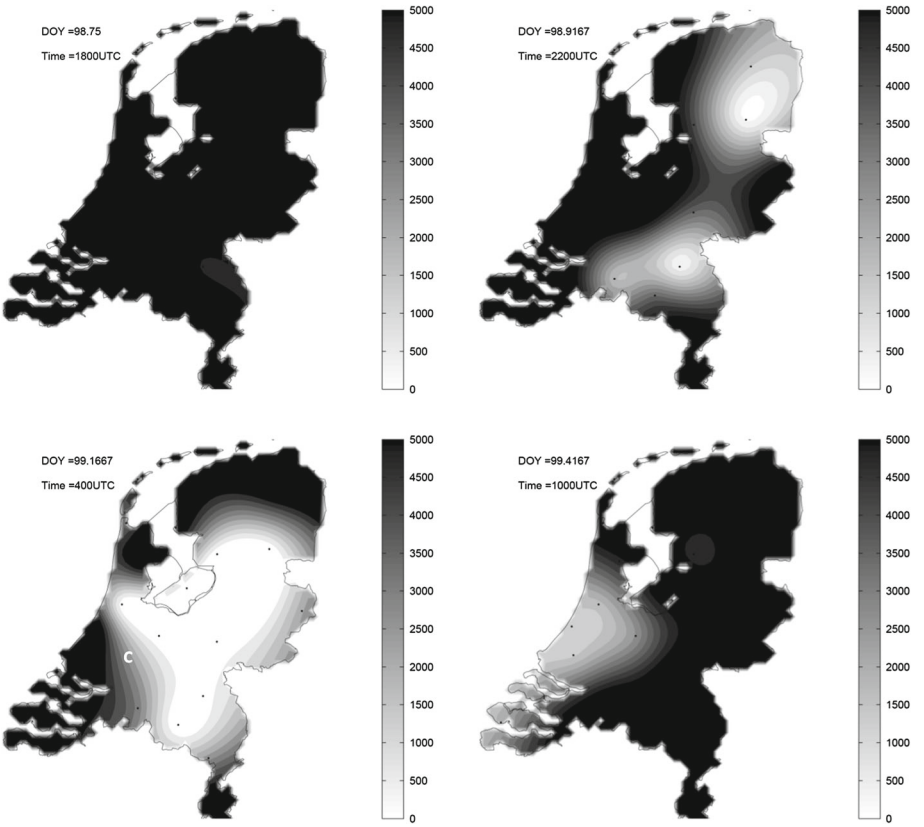

Fig. 4 Observed visibility in the synoptic network over the Netherlands during fog episode 2 (8–9 April 2009). *C* indicates the location of Cabauw

UTC visibility is poor in the central and eastern parts, while on 9 April 2009 at 1200 UTC visibility had improved over the entire country after the passage of the warm front, which induced increased wind speeds and mixing, warming and consequently a decreased RH. For this case the Cabauw tower observations indicate that the fog remained below the 40-m level, and is much thinner than in episode 1.

3 Available Observations

Our model simulations are evaluated against Cabauw tower (Beljaars and Bosveld 1997) and SYNOP observations throughout the Netherlands. The latter provide observed incoming shortwave radiation, 2-m air and dewpoint temperatures, 10-m wind speed and direction, precipitation, visibility, air pressure and cloud cover.

The Cabauw observatory is located in the western part of the Netherlands (51°58′N, 4°56′E, −0.7 m a.s.l.), and consists of a 200-m tower, surrounded by a number of sites dedicated to specialized measurements. The facility is surrounded by an open landscape with grass meadows and ditches, particularly in the westerly direction. The roughness is substantially larger in the easterly direction due to the presence of villages, orchards, and

tree lines. In the southerly and northerly directions, the landscape is a mixture of pasture and windbreaks. The Cabauw facility provides 10-min averaged fluxes of downwelling and upwelling shortwave radiation (ventilated and heated Kipp & Zn CM11 pyranometer), and downwelling and upwelling longwave radiation (Eppley pyrgeometer).

The vertical fluxes of latent heat, sensible heat and momentum were obtained at 5-m height on a site located about 200 m south of the main tower until 13 September 2006, while afterwards these fluxes were observed at 3-m height on a site that is located north of the main tower. These fluxes are obtained using the eddy-correlation technique and stored as 10-min averaged values. High-frequency wind speed and temperature fluctuations were sampled using a Kaijo-Denki TR60-A sonic anemometer until 13 September 2006, which was then replaced by a Gill R3 sonic anemometer. Until 1 November 2005, humidity fluctuations were measured using a KNMI infrared fluctuation meter, which was then replaced by a LICOR-7500 open-path sensor.

Although individual measurement techniques are rather accurate, the surface energy budget at the Cabauw observatory suffers from an imbalance, as has been reported for many other micrometeorological sites worldwide (Foken 2008). At the Cabauw observatory, the available energy during daytime is typically 15 % larger than the sum of the turbulent fluxes (e.g. Steeneveld et al. 2011). During stable stratification, the imbalance in the surface energy budget can amount to 100 % of the net radiation, especially on calm nights.

Air and dewpoint temperatures are measured at heights of 200, 140, 80, 40, 20, 10, and 2 m using a KNMI pt500-element in an unventilated KNMI temperature hut. The dewpoint temperature is derived from RH measurements using a Vaisälä HMP243 heated sensor in a Vaisälä unventilated hut. The temperature measurements have an accuracy of ≈0.1 K, while the accuracy of the RH measurements is about 3.5 %. Hence, the accuracy declines in moister conditions, sometimes resulting in the dewpoint temperature exceeding the air temperature.

The wind speed and direction are measured at 10, 20, 40, 80, 140 and 200 m, as 10-min averages, with wind speed measured using a KNMI cup anemometer, with a diameter of 105 mm and a distance of 100 mm between the centre of the cups and the rotational axis. The wind direction is measured using a wind vane with a distance of 535 mm between both outer sides of the vane.

4 Model Description and Model Set-Up

4.1 The HARMONIE Model

The HARMONIE model is a non-hydrostatic atmospheric model and is the successor of the HIRLAM model (Undén et al. 2002). Its dynamical core originates from the ALADIN model, and solves the fully elastic equations using a semi-Lagrangian discretisation in the horizontal and a hybrid coordinate system in the vertical direction. HARMONIE applies the physical parametrization schemes from the "Application of Research to Operations at Mesoscale" (AROME) model that has been developed by the MESO-NH model community, while the radiation parametrization originates from the European Centre for Medium-Range Weather Forecasts (ECMWF) CY23r4 model. The microphysics are calculated using the ICE-3 package (Pinty and Jabouille 1998), and the shallow convection parametrization is based on the Eddy-Diffusivity Mass-Flux scheme (Siebesma et al. (2007); De Rooy and Siebesma (2008); de Rooy and Siebesma (2010)). The turbulent transport is represented by a prognostic turbulent kinetic energy scheme (Cuxart et al. 2000), while the land-atmosphere coupling uses the surface externalisée scheme (SURFEX; Le Moigne 2012). Land-cover and

surface-parameter values are assigned according to the ECOCLIMAP 1.0 database (Masson et al. 2003).

The HARMONIE model used here has a horizontal computational grid that is centred at Cabauw and contains 300 × 300 grid cells with a grid spacing of 2.5 km. The model utilizes a fine grid spacing in the atmospheric boundary layer (ABL) with the lowest model level at ≈10 m, and six layers in the lowest 200 m. The HARMONIE model obtains its initial and lateral boundary conditions from the ECMWF operational analysis. Simulations of episode 1 were for 5 October 2005, 0000 UTC to 7 October 2005, 0000 UTC, while for the second episode, the simulations start on 8 April 2009, 0000 UTC and finish on 10 April 2009, 0000 UTC.

4.2 The WRF Model

We use the WRF Advance Research Core (ARW, version 3.4.1) non-hydrostatic mesoscale model (Skamarock et al. 2008). Initial and boundary conditions for the WRF simulations have been provided by the ECMWF operational analysis (exactly the same as for the HARMONIE model), while land-use, land-cover, and orography maps have been provided by the U.S. Geological Survey.

To investigate the model sensitivity to domain size, we have set up several different domain configurations. Earlier studies indicated that the performance of limited-area models depend on the domain size (Warner et al. 1997; Leduc and Laprise 2009; Leduc et al. 2011), showing that small-scale atmospheric structures are restricted in their development for a relatively small model domain. Although these studies focussed on the impacts on the middle atmosphere and on precipitation, fog is typically a small-scale process, and modelling results might be sensitive to domain size as well. However, this topic has so far not been studied in the context of fog research. Hence, we first ran the WRF model at the same configuration as the HARMONIE model, i.e. on 300 × 300 points at a spatial resolution of 2.5 km (hereafter referred to as W_P300_R2.5). To evaluate the model sensitivity to domain size and spatial resolution, two additional runs are performed, i.e. one with 150 × 150 points at 5-km resolution (hereafter W_P150_R5) that reveals the impact of spatial resolution, and a second at 300 × 300 points with 5-km resolution (hereafter W_P300_R5), which purely evaluates the impact of domain size.

The WRF model offers the selection of various physical schemes. The tendencies due to shortwave and longwave radiation are estimated using the Dudhia (1989) and the Rapid Radiative Transfer Model (Mlawer et al. 1997), respectively. The Noah land-surface model represents the atmosphere-land coupling (Chen and Dudhia 2001; Chen et al. 2007), which consists of four soil layers with an overlying vegetation layer. In addition, the model sensitivity to the choice of the physical schemes is evaluated. Since we find that the model results of the W_P300_R2.5 run and the W_P150_R5 run are approximately similar, the model sensitivity to physical schemes are performed with the least expensive W_P150_R5 configuration. Special attention is paid to the parametrization of boundary-layer turbulence and microphysics. Our reference runs utilize the Yonsei University (YSU) turbulence scheme and the WRF double-moment 6-class microphysics (WDM6). The sensitivity runs apply the Mellor-Yamada-Nakanishi-Niino 2.5 (MYNN) scheme (Nakanishi and Niino 2006) and the single-moment schemes WSM3 and WSM6.

Finally, we study the influence of grid nesting, by performing a set of runs with a model domain of 60 × 60 cells, covering 1,500 km × 1,500 km at a resolution of 25 km (domain size as W_P300_R5), in which we nest a domain of 150 × 150 grid cells, covering 750 km × 750 km at 5-km resolution. The inner domain results for these simulations are compared to the

W_P150_R5 run. Also, the runs with the nested domain are executed once with one-way nesting and once with two-way nesting, and differences are reported.

5 Results for Episode 1: 5–7 October 2005

5.1 Times Series and Vertical Structure

Here we present the modelling results for the surface energy and radiation fluxes. For clarity, the initial profiles in the WRF and the HARMONIE models are identical, since they are based on the same ECMWF operational analysis. All WRF model configurations represent the diurnal cycle of net radiation (Q^*) reasonably well. At noon of October 5, Q^* is overestimated by about 40 W m^{-2} (Fig. 5a), and during the subsequent night Q^* in the WRF model has a negative bias of about 20 W m^{-2} before the fog episode starts. The modelled fog onset occurs around 6 October 2005, 0400 UTC, which is correctly timed compared to the observations. Subsequently Q^* slowly decreases to zero, while the following day the modelled Q^*increases more rapidly than observed, indicating that the WRF model dissipates the fog more rapidly than was observed. Apparently the modelled fog was optically less thick than the observed fog, as is confirmed later by analyzing the thermodynamic profiles. The shortwave downwelling radiation ($S^{\downarrow}$) is simulated correctly, except for the early fog dissipation on the morning of 6 October (Fig. 5b). The simulated longwave downwelling radiation ($L^{\downarrow}$) under clear sky and fog-free conditions experiences a negative bias of about 10–20 W m^{-2}, which is independent of the model configuration (Fig. 5c). Analogous studies found the same bias (Van der Velde et al. 2010; Steeneveld et al. 2011; Kleczek et al. 2014; Bosveld et al. 2014), the last authors arguing that the bias is due to the model's misrepresentation of temperature and moisture profiles in the ABL. In addition, Wild et al. (2001) found that this bias is most prominent for stable and for cold conditions, which is confirmed in our study. The W_P300_R5 configuration, with the largest model domain, has a slightly higher $L^{\downarrow}$ than the WRF runs with the smaller domain. This is consistent with the slightly warmer and more humid atmosphere than was observed (see Fig. 7b). The sudden increase in $L^{\downarrow}$ at 0400 UTC on 6 October due to the fog formation is captured by the WRF model, although the $L^{\downarrow}$ increase by the WRF model is larger than was observed. Although the modelled $L^{\downarrow}$ agrees with the observations, the modelled fog was thinner than observed (see Fig. 7d). This implies that either the modelled fog depth was optically thicker than observed, or that the model is also subject to a bias in cloudy conditions. In this case, the latter is most likely since the vertical profiles of dewpoint depression indicate that the observed fog was deeper than predicted (Figs. 6d, 7). The model behaviour of the upward longwave radiation follows that of the surface skin temperature (T_{sk}), with a correct daytime representation by the WRF model, and a negative bias of $\approx$20 W m^{-2} by the HARMONIE model. At night, the HARMONIE model results show the highest $L^{\uparrow}$ values, which is consistent with high T_{sk} (Fig. 6c). Finally, it is striking that W_P300_R2.5 also forecasts fog from 6 October, 1800 UTC, while fog was not observed, and not forecast by the other simulations. The 2-m air temperature (T_2) in the W_P300_R2.5 run is slightly higher than was observed, and than was forecast by the other model runs, and therefore the recurrent fog must be caused by a moist bias (Fig. 6e). This bias can be explained by a zero latent heat flux in the W_P300_R2.5 run, while the other permutations indicate a dewfall of 15 W m^{-2}, which substantially reduces the atmospheric moisture content. This run also does not reach a substantial degree of near-surface stability, with a marginal sensible heat flux.

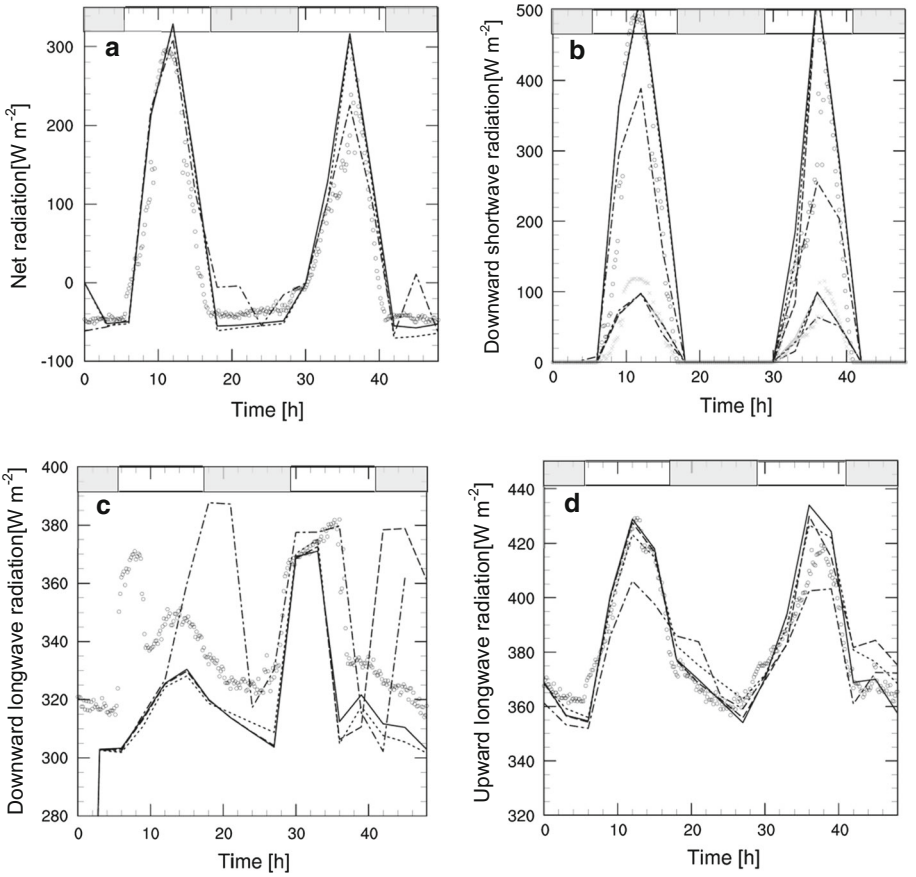

Fig. 5 Modelled (WRF and HARMONIE) and observed (Cabauw, *circles*) time series of net radiation (**a**), shortwave radiation (**b**), longwave downward radiation (**c**), and longwave upward radiation (**d**) for the period 5 October 2005, 0000 UTC to 7 October 2005, 0000 UTC. *Full line* W_P300_R2.5; *dash* W_P150_R5, *dot* W_P300_R5; *dash-dot* HARMONIE. The *grey shading* at the top of the graph indicates a nighttime period

Concerning near-surface variables, the WRF model forecasts T_2 very well until fog formation (Fig. 6a); subsequently, the three configurations clearly diverge, with W_P300_R5 reaching highest T_2 values. Run W_P150_R5 shows the best performance during the daytime of 6 October, while the P300 runs then overestimate T_2 substantially by $\approx$3 K, suggesting that the P300 runs dissipate the fog too quickly in the morning. Also note that the amplitude of the diurnal cycle of T_2 is underestimated in the HARMONIE model.

The 10-m wind speed is overestimated by all runs (Fig. 6b). At noon on October 5 the model produces a wind speed of $\approx 5\,\mathrm{m\,s^{-1}}$ while typically $3.5\,\mathrm{m\,s^{-1}}$ was observed. The observations indicate a rapid decrease in wind speed between 1400 and 1600 UTC, while the model follows this decrease more slowly, creating a relatively large bias. During the fog episode, between 0400 and 1200 UTC on 6 October, the wind forecast is satisfactory, while during the following day the wind speed is overestimated by $\approx 1.5\,\mathrm{m\,s^{-1}}$. Similar results are found for the friction velocity (u_*) with a substantial overestimation during daytime ($0.28\,\mathrm{m\,s^{-1}}$ observed vs. $0.55\,\mathrm{m\,s^{-1}}$ simulated). The remarkable decrease in u_* at the start of the night of 5–6 October is missing in the model results. Therefore, it is remarkable that

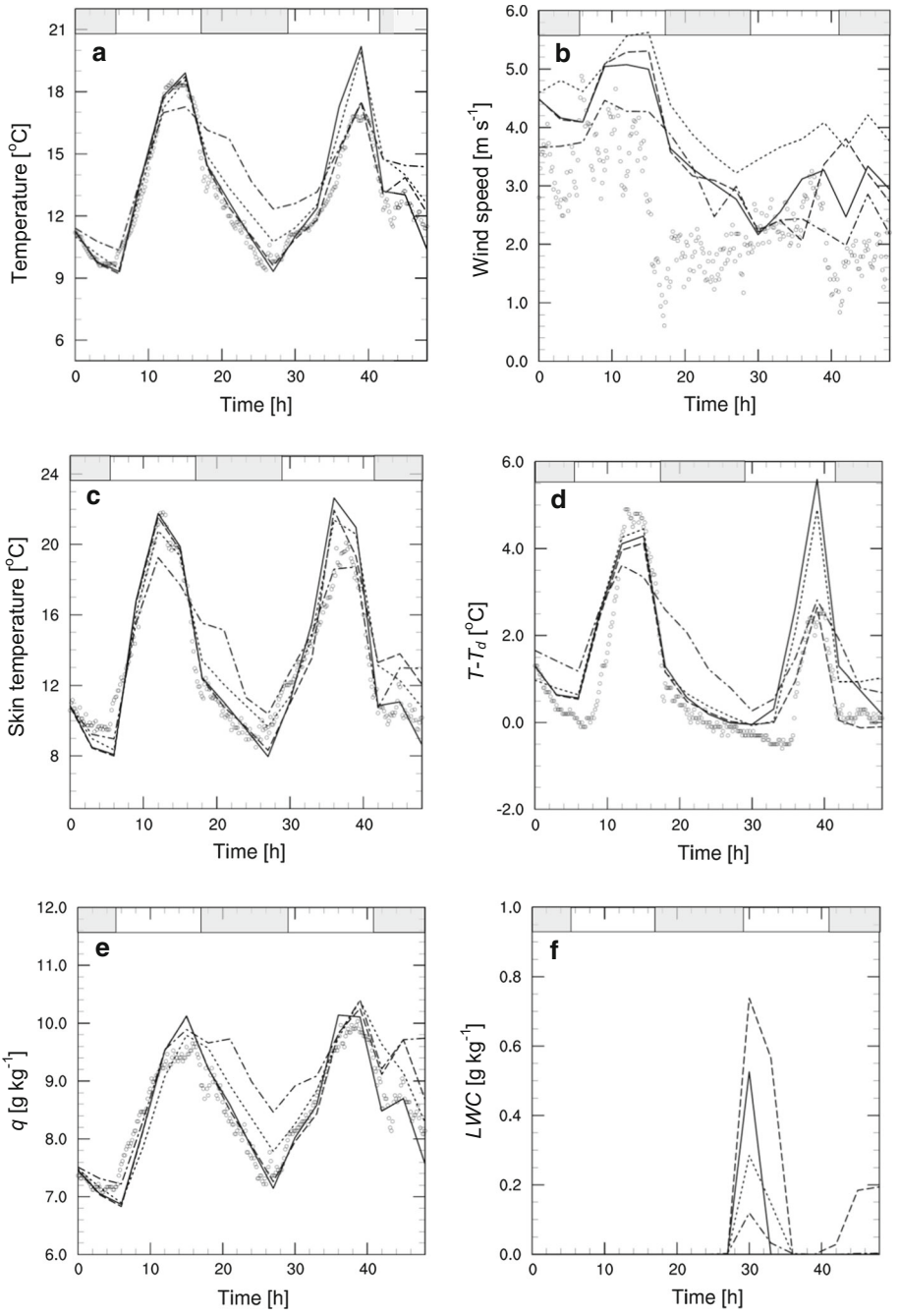

Fig. 6 Modelled (WRF and HARMONIE) and observed (Cabauw, *circles*) 2-m temperature (**a**), wind speed (**b**), skin temperature (**c**), dewpoint depression (**d**), specific humidity (**e**), and liquid water content on the first model (**f**) for the period of 5 October 2005, 0000 UTC to 7 October 2005, 0000 UTC. *Full line* W_P300_R2.5; *dash* W_P150_R5, *dot* W_P300_R5; *dash-dot* HARMONIE. The *grey shading* at the top of the graph indicates a nighttime period

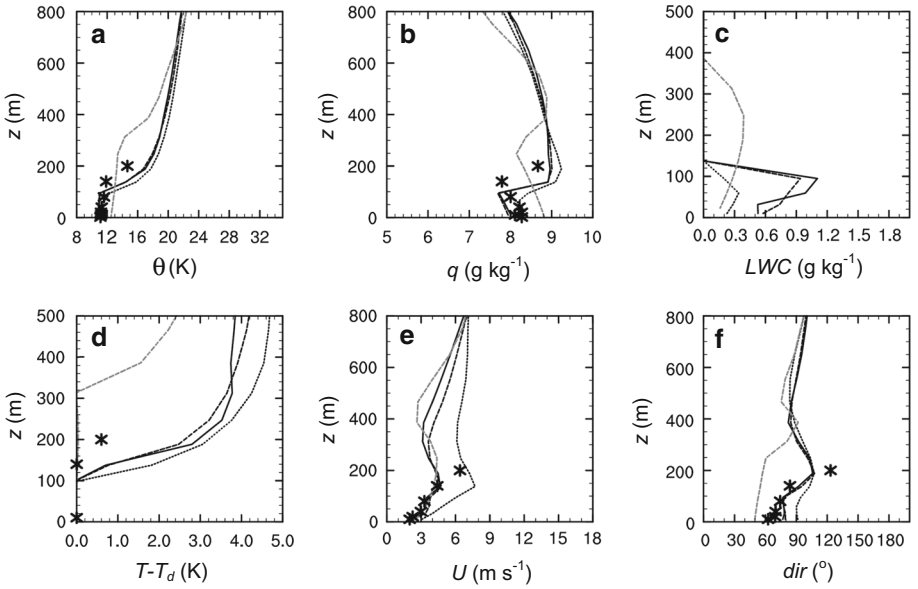

Fig. 7 Modelled (WRF and HARMONIE) and observed (Cabauw, *asterisk*) vertical profiles of potential temperature (**a**), specific humidity (**b**), liquid water content (**c**, no obs available), dewpoint depression (**d**), wind speed (**e**), and wind direction (**f**) for October 6, 0600 UTC. *Full line* W_P300_R2.5; *dash* W_P150_R5, *dot* W_P300_R5; *grey dash* HARMONIE

the model forecasts the fog reasonably well, whereas it does not forecast the quiet period preceding the fog episode. During the fog episode, u_* increases due to enhanced mixing in the fog layer, found in the P300 runs, while in the P150 runs u_* increases more slowly, but its decrease at night is not seen.

The 2-m specific humidity (q_2) correctly follows the observations, except after 6 October at 1800 UTC, where W_P150_R5 and W_P300_R5 runs overestimate q_2 by $\approx 1\,\mathrm{g\,kg^{-1}}$. As such the correct q_2 serves as a good basis for accurate liquid water content (*LWC*) forecasting (Fig. 6f). Unfortunately *LWC* values are not recorded at the Cabauw site, and thus we can only distinguish the modelled *LWC* between available configurations. W_P300_R2.5 forecasts a maximum *LWC* value of $0.6\,\mathrm{g\,kg^{-1}}$ at midnight on October 6. Despite the timing of the fog onset being similar in W_P300_R5, its peak *LWC* value occurs later, i.e. on 6 October at 0900 UTC. Finally the W_P150_R5 run re-initiates fog around 6 October 2005 at 1800 UTC in the evening while this was not observed at that time.

The HARMONIE model results clearly differ from the WRF model results for this case. In general, the diurnal cycle of T_2 and T_{sk} (not shown) is dampened compared to WRF simulations and compared to the observations. In addition, the HARMONIE model forecasts q_2 well in the first 12 h, but after 5 October 2005 at 1200 UTC q_2 values are overestimated by $\approx 1.5\,\mathrm{g\,kg^{-1}}$. This occurs only very close to the surface, while the HARMONIE model follows the WRF model calculations closely above 200 m (not shown). The consequence of the warm and moist bias is a near-surface dewpoint depression that decays too late and reaches its minimum value around 6 October 2005 at 0200 UTC, which is still ≈ 0.5 K higher than in the WRF model runs. During the following day the HARMONIE model follows the observed dewpoint depression whereas the WRF model overestimates it by ≈ 3 K. Another important finding is that the wind speed in the HARMONIE model is typically $0.5\,\mathrm{m\,s^{-1}}$

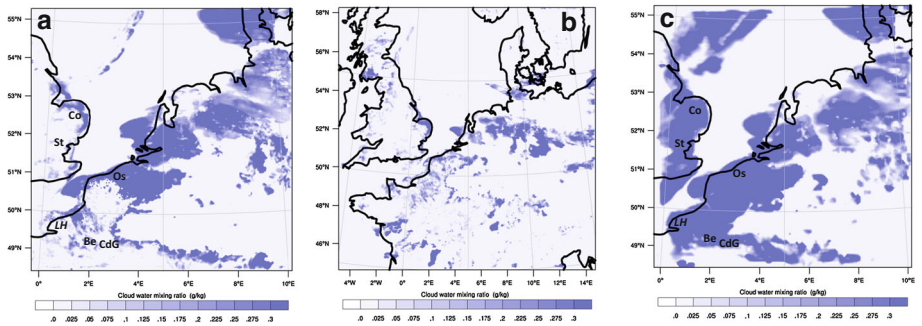

Fig. 8 WRF modelled fog liquid water content at the first model level (g kg^{-1}) on October 6 2005, 0600 UTC. **a** W_P300_R2.5, **b** W_P300_R5, **c** W_P150_R5. Weather stations: Coltishall (Co), Stansted (St), Ostend (Os), Le Havre (LH), Beauvais (Be), and Charles de Gaulle (CdG) are indicated in **a** and **c**. See text for detailed discussions of the fog observations

higher than in the WRF model, while u_* is overestimated by the HARMONIE model from 6 October, 0200 UTC onwards, by $\approx$0.05 m s^{-1}. The reason that the HARMONIE model results differ from the WRF model results is because the HARMONIE model develops a shallow stratus layer between 500 and 800 m from 5 October, 1200 UTC, as is clearly seen in the vertical profile of the dewpoint depression and in $L^{\downarrow}$ that is about 60 W m^{-2} higher than observed. Towards the following night the HARMONIE model lowers the stratus layer, leading to fog formation. Consequently the sensible heat flux is only 30 W m^{-2} at noon, while 90 W m^{-2} was observed, and the WRF model produced values of $\approx$110 W m^{-2} (not shown).

Considering the modelled vertical profiles, both models generate a strong stratification close to the surface before the fog onset (not shown), but with small differences between the runs. After the fog onset all WRF runs indicate a well-mixed layer of $\approx$100 m deep (6 October 2005, 0600 UTC), with a potential temperature similar to that observed (Fig. 7a). However, the observed well-mixed fog layer is $\approx$60 m deeper than forecast (Fig. 7d). The HARMONIE model simulates a well-mixed profile with a fog depth of $\approx$300 m, though the development of the fog layer differs from that in the WRF model, i.e. an analysis of a series of vertical profiles as forecast by the HARMONIE model run indicates that the fog commences with a stratus layer that is lowered during the night. The deeper mixing and the raised inversion in the HARMONIE model are also reflected in the specific humidity (q, Fig. 7b); decreasing q values with height are successfully reproduced by the WRF model, though over a thinner layer than that observed. Note that the modelled inversion strength approaches the observed strength closely. The q profile of the W_P300_R5 run deviates slightly from the other WRF model runs and produces q values that increase with height. The HARMONIE model simulates a much deeper layer of decreasing q with height, with the humidity inversion between 300 and 400 m. The modelled *LWC* values show a maximum at the top of the fog layer in the WRF model runs with the smallest domain and amount to $\approx$1 g kg^{-1}, while W_P300_R5 produces much smaller *LWC* values $\approx$0.28 g kg^{-1} (Fig. 8c). The wind speed is reasonably reproduced by the HARMONIE model and the WRF model runs with a small domain (Fig. 7e). Moreover it is interesting to note that the wind profiles differ slightly above the fog layer, which likely indicates that the different runs are in a different phase of the inertial oscillation. Finally, the wind direction is also best reproduced by the WRF model with the small domain, while the HARMONIE model has a wind profile with a stronger backing than that observed and from the WRF runs (Fig. 7f). On the contrary, the

wind direction in the W_P300_R5 run is veered by about 20° with respect to the observations near the surface.

5.2 Spatial Variation

Figure 8 shows the model sensitivity of forecast *LWC* on the first model level to domain size and grid resolution for 6 October 2005,0600 UTC. Our reference run W_P300_R2.5 forecasts fog in a wide area of the Netherlands and Belgium, analogous to the observations. Using an identical model domain size, but with coarser spatial resolution (W_P150_R5), the spatial coverage of the forecast fog in the Netherlands and western Germany is approximately similar to the results of W_P300_R2.5, although the (probably not verifiable) spatial detail has been reduced. Note that both runs produce about the same *LWC* magnitude over the Netherlands, with *LWC* values $\approx 0.3\,\mathrm{g\,kg^{-1}}$ for areas with well-developed fog. The main differences between runs W_P150_R5 and W_P300_R2.5 occur above England, the northern North Sea and the coastal areas of Belgium and Northern France.

For those regions, we briefly summarize the observations (see weather stations in Fig. 8), and compare these with the model results. Routine synoptic observations from weather station Coltishall (north-eastern Norfolk, UK) reported fog between 0450 and 0550 UTC, and between 0520 and 0650 UTC Stansted airport (near London, UK) observed fog as well. Lille (France) registered fog between 0300 and 1030 UTC, and between 0020 and 0900 UTC Ostend (Belgium) reported fog, and a more inland station, Beauvais (Belgium) reported fog between 0430–0900 UTC. To the south, Le Havre (French coast) did not report any fog, though north-east of Paris, Charles de Gaulle airport reported fog from 0200 UTC to 0930 UTC.

Considering these observations, the coarse resolution model run W_P150_R5 seems to perform slightly better than the fine resolution run W_P300_R2.5. In particular the W_P150_R5 run forecasts the fog further south than W_P300_R2.5, which is in better agreement with the observations. Run W_P300_R5 provides substantially different results than the two other runs. Particularly the fog occurs in a more patchy character over Belgium, and a much thinner fog field in the west of the Netherlands. These results correspond to Warner et al. (1997) and Leduc and Laprise (2009) and Leduc et al. (2011) who found that limited area models are better at developing small-scale structures when the domain size increases. Moreover the fog amount at the U.K. east coast is confined to a much smaller region than in W_P150_R5 (Fig. 8).

5.3 Physical Parametrizations

Next, we study the sensitivity of the model skill to the selected physical parametrizations. Six sensitivity runs in which the YSU scheme (Fig. 9a, c, e) was permutated with the MYNN scheme (Fig. 9b, d, f), and the WDM6 parametrization (Fig. 9e, f) was permutated with the WSM3 (Fig. 9a, b) and WSM6 parametrizations (Fig. 9c, d).

Clearly, the boundary-layer scheme is the critical part in forecasting radiation fog in the area around Cabauw. Runs using the YSU scheme generate fog, while fog is lacking in runs with the MYNN scheme (e.g. Fig. 9a,b). A closer analysis reveals that this difference is caused by subtle differences in the modelled temperature and humidity profiles that originate from a stronger turbulent mixing in the MYNN scheme than in the YSU scheme. The MYNN parametrization generates the highest latent heat flux during the day preceding fog formation, and therefore at first sight MYNN results appear favourable for fog formation. However, the surface cooling by the two schemes is approximately similar, but this cooling is mixed over a

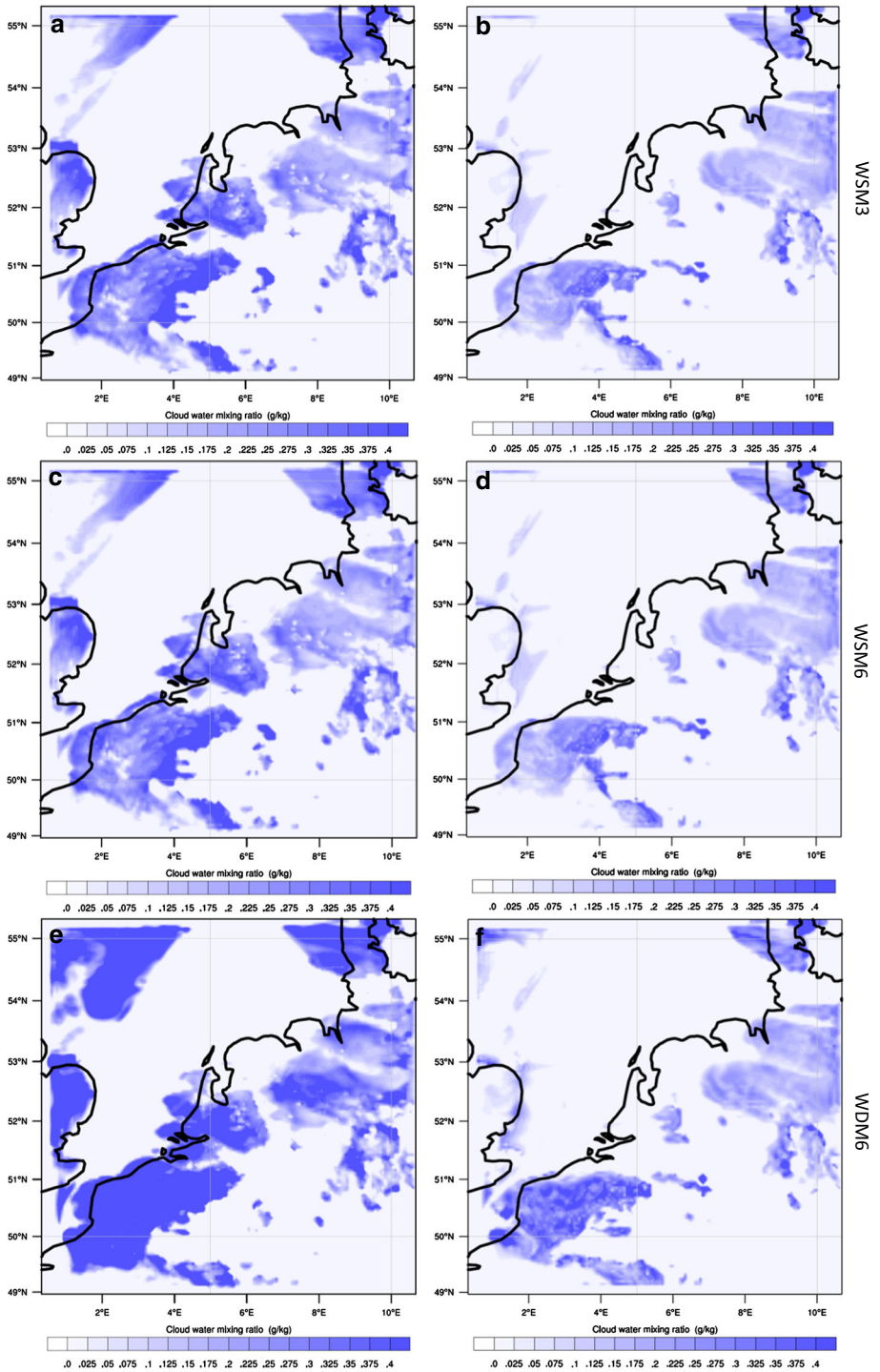

Fig. 9 Modelled liquid water content ($g\,kg^{-1}$) at the first model level for 6 October 2005, 0600 UTC in the W_P150_R5 configuration for a variety of PBL schemes and microphysical schemes. *Left* YSU; *right* MYNN

deeper layer in the MYNN simulation than in the YSU simulation, since the simulated ABL using the MYNN scheme is about 50–100 m deeper than in the YSU scheme. Consequently, above the 100-m level the dewpoint depression between 100 and 300 m is about 0.5 K smaller with MYNN than with YSU, while below 100 m the dewpoint depression was 0.2 K smaller than in YSU. This relatively small difference is apparently sufficient to prevent the fog onset.

For the more south-westerly located area around Lille (France), the fog is reasonably well generated with either the YSU or the MYNN scheme, although the fog onset is ≈2 h earlier than observed. We consider this still as a good match, considering the complexity involved in fog forecasting. Fog was first observed 0400 UTC and the fog dissipated around 1130 UTC. The most prominent difference between the runs occurs at the time of the fog dispersal, where the MYNN scheme dissipates the fog at 6 October, 1200 UTC, while with the YSU scheme the fog persists for the remainder of the model run. YSU has its maximum *LWC* value $>1\,\mathrm{g\,kg^{-1}}$ at 6 October, 1200 UTC.

The differences in the model results for permutations for the microphysical scheme depend on the amount of fog itself. For relatively small *LWC* values, as with the MYNN scheme (Fig. 9b, d, f) the sensitivity to the microphysical scheme is rather limited. The differences are marginal between runs using WSM3 and runs using WSM6. This can be explained by the fact that the fog is termed a warm fog and the condensed water species are dominated by liquid water in all cases. Comparing the results of the single-moment schemes WSM3 and WSM6 with the double-moment scheme WDM6, we find substantially higher *LWC* values with the latter.

5.4 Nesting

Grid nesting is often applied to avoid computationally expensive runs of the W_P300_R2.5 type. To study the impact of nesting on the representation of the fog, the WRF model is operated with a set-up of the relatively successful W_P150_R5 configuration, but with additional nesting. An outer domain was defined of 61 × 61 cells with a resolution of 25 km. Herein one domain is nested with 150 × 150 cells and a resolution of 5 km.

Considering the October episode, only marginal differences are found between the forecasted fog field, with the near-surface *LWC* values of the nested runs being rather close to the results of the W_P150_R5 run. In addition, model results from one-way and two-way nesting results correspond well (not shown).

6 Results for Episode 2: 8 and 9 April 2009

6.1 Time Series and Vertical Structure

The modelled time series for the April case shows a reasonable agreement with the observations, but for certain micrometeorological variables we find substantial biases. Also, slight differences appear in the results of the different model configurations. In this section we discuss the model performance for the Cabauw site.

The incoming solar radiation ($S^{\downarrow}$) in the WRF model peaks at $\approx 600\,\mathrm{W\,m^{-2}}$ while the observations indicate a maximum of $\approx 300\,\mathrm{W\,m^{-2}}$ on the first day (Fig. 10b). As such, the developing clouds appear later in the model than in the observations, which is consistent with the delayed increase of $L^{\downarrow}$ as compared to the observations (Fig. 10c). On the second day, the WRF model results indicate a clear sky since the forecast $S^{\downarrow}$ follows a smooth curve, with a maximum of $700\,\mathrm{W\,m^{-2}}$ at noon, whereas the observations indicate a highly

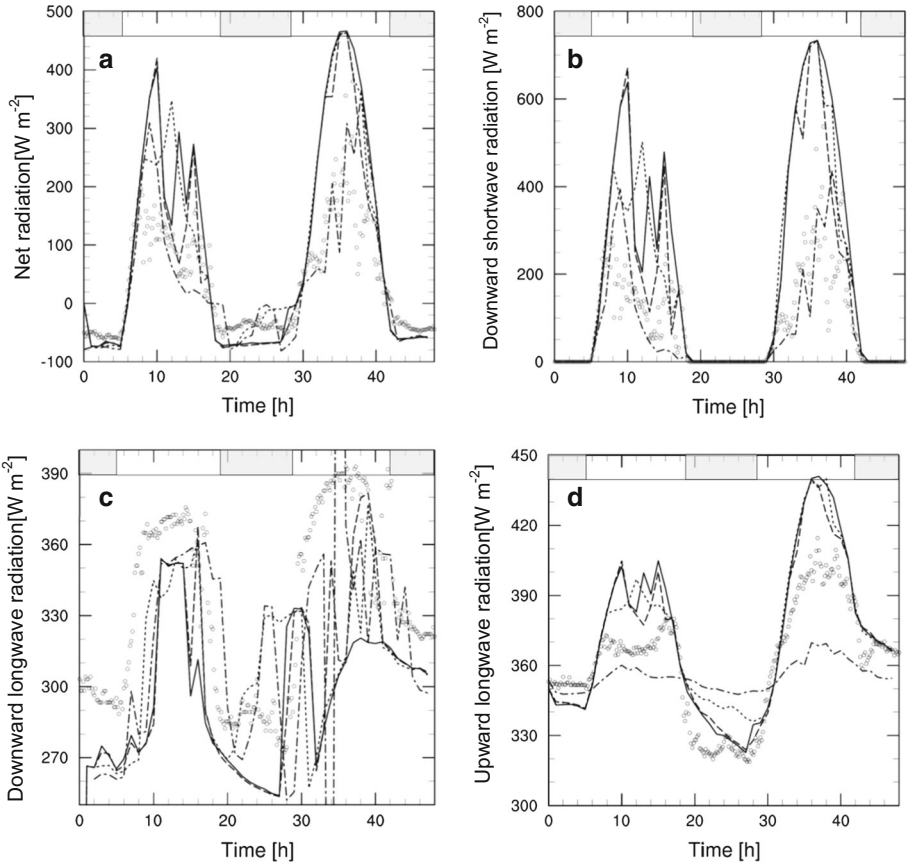

Fig. 10 Modelled (WRF and HARMONIE) and observed (Cabauw, *circles*) time series of net radiation (**a**), shortwave radiation (**b**), longwave downward radiation (**c**), and longwave upward radiation (**d**) for the period of 8 April 2009, 0000 UTC to 10 April 2009, 0000 UTC. *Full line* W_P300_R2.5; *dash* W_P150_R5, *dot* W_P300_R5; *dash-dot* HARMONIE. The *grey blocks* at the top of the graph indicates a night-time period

variable $S^{\downarrow}$ over the day, suggesting the presence of scattered clouds. Consequently, the modelled Q^* is substantially higher than that observed on both days (Fig. 10a), resulting in an overestimation of T_{sk} by $\approx$3 K during the daytime. At night the simulated minimum temperature is approximately correct; T_{sk} falls more slowly in the WRF model runs than in reality, which shows a very rapid fall immediately after the evening transition (Fig. 11c).

The T_2 has been well forecast (Fig. 11a), particularly at night, which is surprising since simulation of the stable boundary layer is usually challenging for a limited-area model (e.g. Holtslag et al. 2013). During both daytime periods, the three WRF model configurations overestimate T_2 values by about $\approx$3 K, being consistent with the overestimated $S^{\downarrow}$ by the WRF model. Obviously, the diurnal cycle of T_2 is underestimated in the HARMONIE model, with underestimated nocturnal cooling and $\approx$4 K cold bias during the second day. This underestimation is consistent with our findings for episode 1. In all runs, the modelled 10-m wind speed follows the observations closely (Fig. 11b), and even the fall in the 10-m wind speed around 1800 UTC is well captured. During the second day the models underestimate the wind speed by about 2 m s^{-1}. Apparently all schemes

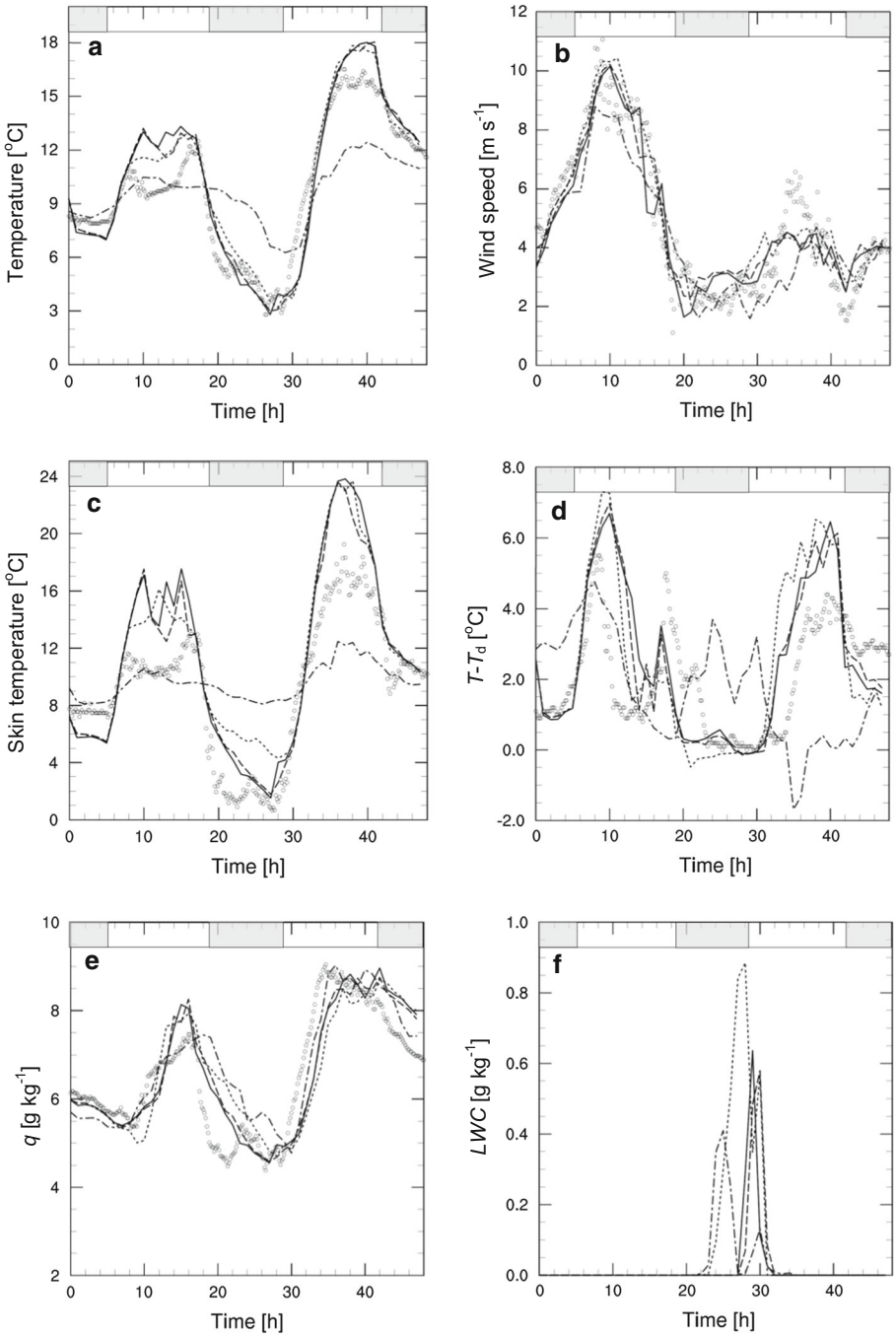

Fig. 11 Modelled (WRF and HARMONIE) and observed (Cabauw, *circles*) 2-m temperature (**a**), wind speed (**b**), skin temperature (**c**), dewpoint depression (**d**), specific humidity (**e**), and liquid water content at the first model level (**f**) for the period of 8 April 2009, 0000 UTC to 10 April 2009, 0000 UTC. *Full line* W_P300_R2.5; *dash* W_P150_R5, *dot* W_P300_R5; *dash-dot* HARMONIE. The *grey shading* at the top of the graph indicates a nighttime period

underestimate the mixing intensity of the boundary-layer turbulence. In addition, the wind-speed increase as forecast by the HARMONIE model was delayed compared to the wind-speed increase in the WRF model and the observations. The observed, very sharp, fall on the next evening around 1800 UTC is also captured by both models, although the fall occurs about 2 h later in the HARMONIE model than that observed. Moreover, the minimum wind speed is overestimated by $\approx 1\,\mathrm{m\,s^{-1}}$ in the WRF model as compared to the observations.

The modelled q_2 follows the observations to a great extent (Fig. 11e), except that the modelled diurnal cycle shows delays in both the morning and evening transition. The delayed surface cooling results in delays in the modelled dewfall, and therefore the simulated q_2 values remain high, especially in W_P300_R5. The HARMONIE model result closely follows the W_P300_R5 simulation, with a moist bias during the night. Consistent with the delayed cooling, the 2-m dewpoint depression declines earlier in the WRF model than that observed. Note that the WRF model represents the observed peak in dewpoint depression on 8 April 2009 at 1800 UTC relatively well (Fig. 11d). The reduced cooling as provided by the HARMONIE model is responsible for a dewpoint depression of ≈ 3 K, and as such hampers fog formation in that model. The highest *LWC* value is achieved with the largest domain set-up (W_P300_R5) and amounts to 0.9 $\mathrm{g\,kg^{-1}}$, while the other WRF model runs forecast a *LWC* value of 0.6 $\mathrm{g\,kg^{-1}}$ (Fig. 11f). This is most likely caused by the reduced dewfall in W_P300_R5 where the latent heat flux is nearly zero between 1800–2300 UTC (not shown), while the other WRF model permutations have a latent heat flux of about $-10\,\mathrm{W\,m^{-2}}$ in that period. This difference is a consequence of the limited T_{sk} fall in that simulation. The W_P300_R5 run also initiates the fog ≈ 4 h earlier than in the two other runs, which is also closest to the observations reporting fog from midnight to 0600 UTC. The HARMONIE model results do not indicate any fog.

Finally, we discuss the representation of the vertical structure of this fog on 9 April 2009 at 0600 UTC (Fig. 12a–f). A strong inversion of ≈ 4.5 K is observed between 200 m and the surface (Fig. 12a). The HARMONIE model produces a log-linear potential temperature profile that indicates the lack of fog. The WRF model permutations already produce a fog layer with a depth of ≈ 100 m (Fig. 12c), with the highest *LWC* value modelled by the W_R300_P2.5 run. The observed dewpoint depression indicates a very thin fog with a substantially dryer layer aloft (Fig. 12d). The WRF model runs overestimate the fog at this time, as is also seen by the $L^{\downarrow}$ increase ahead of the time compared to the observations (Fig. 10c). Note that two runs, i.e. W_P300_R2.5 and W_P150_R5, reproduce the $L^{\uparrow}$ values well, particularly at night. However, the W_P300_R5 simulation performs relatively meagre compared to the other WRF model runs. Remarkably, the HARMONIE model runs substantially underestimate the amplitude of the diurnal cycle of $L^{\uparrow}$ (Fig. 10d).

Although the HARMONIE model simulation reproduces the steep gradient of the dewpoint depression, it overestimates this quantity around the 300-m level. Although all models reasonably reproduced the 10-m wind speed, the vertical profiles of wind speed differ substantially (Fig. 12e). In the W_P300_R5 simulation, the wind speed is $\approx 2\,\mathrm{m\,s^{-1}}$ higher than in its two WRF model counterparts above the fog layer. In the HARMONIE model the wind speed is successfully estimated below the 200-m level, while the wind speed aloft is overestimated substantially. The wind direction in the WRF model corresponds to the observations, while the wind turning between the surface and the 200-m level amounts to several tens of degrees more in the HARMONIE model than that observed (Fig. 12f).

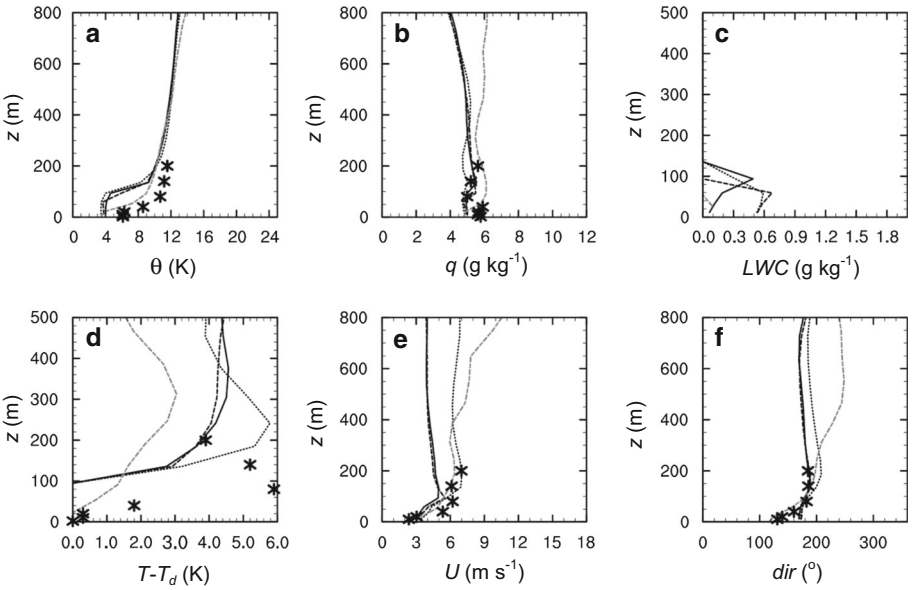

Fig. 12 Modelled (WRF and HARMONIE) and observed (Cabauw, *asterisk*) vertical profiles of potential temperature (**a**), specific humidity (**b**), liquid water content (**c**, no obs available), dewpoint depression (**d**), wind-speed magnitude (**e**), and wind direction (**f**) for 9 April 2009, 0600 UTC. *Full line* W_P300_R2.5; *dash* W_P150_R5, *dot* W_P300_R5; *grey dash* HARMONIE

6.2 Spatial Variation

We find that the fog onset occurs earlier in the W_P300_R5 run than in the other WRF model runs with the smaller domain size. For instance, on 8 April 2009 at 2100 UTC scattered fog is already generated in W_P300_R5 and not in the other runs (not shown). This occurs both over the north-eastern portion of the Netherlands and over the North Sea. At midnight, W_P300_R5 simulates widespread fogs over the Netherlands and the southern North Sea, while the runs with the smaller domain produce only scattered fog patches (not shown). In addition, the latter runs create patches that are spatially relatively homogeneous compared to the W_P300_R5 run that indicates larger-scale fog fields, but with patches of smaller *LWC* values, that appear to start from the centre of the large fog field, while keeping the edges of the fog field intact. At around 0400 UTC on April 9, this structure of the fog fields is also found in the two other runs. In general the differences between the model runs as found for the October case are confirmed, with approximately similar results for the simulations with the same domain size (Fig. 13). The fog field is most scattered in the simulation with the highest resolution, although these differences are hard to confirm from field observations. Surprisingly, at 0900 UTC, the W_P150_R5 simulation produces a large fog field over the North Sea adjacent to the English east coast, while fog is absent in the W_P300_R5 simulation, and much less intense in the W_P300_R2.5 simulation.

6.3 Nesting

In this case, the impact of nesting is different than for the October case. It appears that the fog develops earlier in the nested run than in the run with a single domain (not shown), while

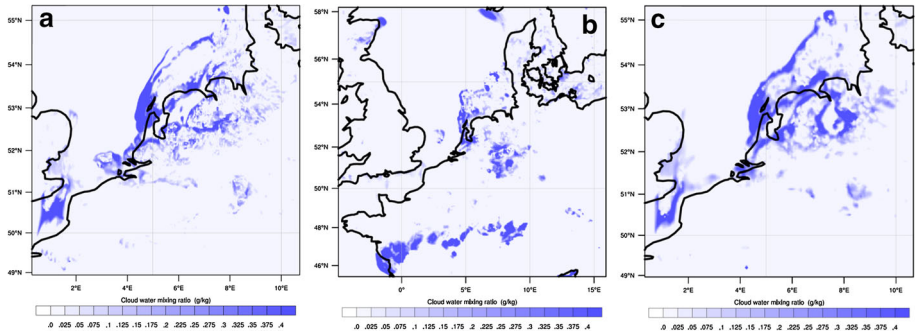

Fig. 13 Modelled fog liquid water content on the first model level on 9 April 2009, 0600 UTC. **a** W_P300_R2.5; **b** W_P300_R5; **c** W_P150_R5

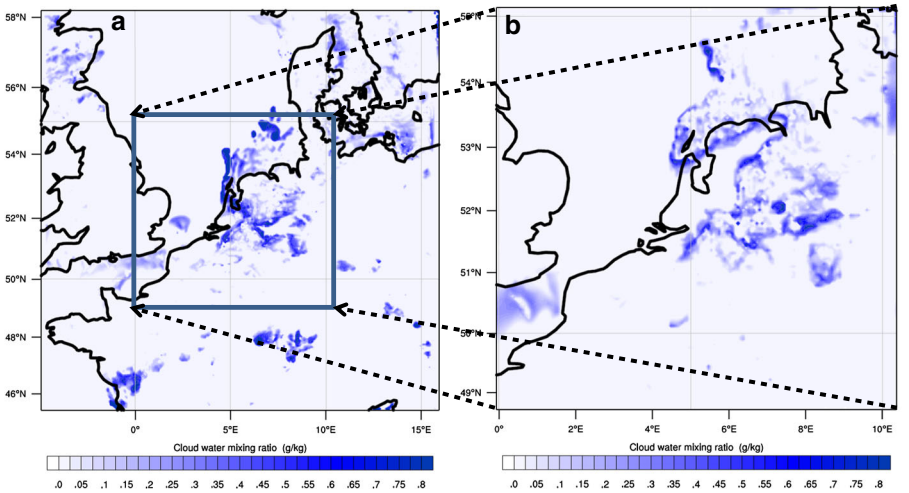

Fig. 14 Modelled liquid water content at the first model level for 9 April 2009, 0300 UTC for run W_P300_R5 (**a** no nesting) and for a run with a nested domain 5-km resolution (**b**)

the maximum fog extent is largest in the nested runs. At midnight the nested run produces a large area from southwest to northeast with *LWC* values between 0.6 and 0.8 g kg^{-1}. This line develops 3 h later in the W_P150_R5 run, i.e. around 9 April 2009 at 0300 UTC, but with a smaller *LWC* value of 0.2 g kg^{-1}. In the runs with nesting, the fog layer becomes unstable quickly after midnight, and therefore the *LWC* at the lowest model level is reduced suddenly between 0100 and 0200 UTC, and therefore fog is not forecast at the Cabauw site (Fig. 14). The model results between one-way and two-way nesting are again in close agreement, and as such this experiment confirms the results for the October case.

7 Conclusion

We have evaluated the operational WRF and HARMONIE mesoscale models for two different warm fog episodes that were observed at the Cabauw research tower facility in the

Netherlands. One fog case occurs in a long lasting calm autumn episode, and in the second case fog develops in calm clear-sky conditions after the passage of a cold front in spring. In addition, we evaluate the sensitivity of the WRF model results to the selection of the boundary-layer and the microphysical parametrizations. Finally, the role and influence of spatial resolution, domain size and nesting is evaluated.

The reference WRF run for the autumn case, which uses the YSU boundary-layer scheme and the WDM6 microphysical scheme, successfully forecasts radiation fog with an approximately correct timing of the onset. However, the developed fog layer is about 100 m thinner than was observed, and consequently the fog dissipation in the morning occurs too early in the model. In contrast, the HARMONIE model forecasts fog of a completely different fog archetype than that observed, i.e. a so-called "stratus lowering fog" that is about twice as deep as was observed. As such, the modelled radiation and energy balances and vertical structure differ substantially in the WRF and the HARMONIE models.

Within the WRF model we find that the fog forecast with 2.5-km and 5-km spatial resolutions provide similar fog onset and spatial extent. Using a larger model domain results in more scattered fog than with a small domain, while the results with the smallest domain represent reality most closely. Considering the sensitivity to the parametrization we find that a single-moment microphysical scheme forecasts a lower *LWC* values than does the double-moment scheme. Also, simulations with the YSU boundary-layer scheme provide more widespread fog fields with a higher *LWC* than with the MYNN scheme. Finally, our experiments indicate a considerable impact of the inclusion of nested domains in the mother domain. Nesting appears to deteriorate the fog formation in the model, and as such we recommend fog forecasting in a single domain with a spatially high resolution.

Simulations for the spring case confirm the general model behaviour of the autumn case. Again, the fog onset in the WRF model is reasonable, though the fog is slightly deeper than was observed. The HARMONIE simulation does not represent the fog due to a substantial dewpoint depression, as a result of a warm bias in the 2-m air temperature. Overall, fog forecasting remains a challenging task with results depending on subtleties in the formulation of the physical processes as well as technical aspects such as domain size and grid nesting.

Acknowledgments The authors thank the Royal Netherlands Meteorological Institute for providing Dutch meteorological network data and Cabauw tower data. Reinder Ronda acknowledges financial support of Knowledge for Climate research project "IMPACT". The contribution by G.J. Steeneveld has been sponsored by the NWO contract 863.10.010 (Lifting the fog). This work was sponsored by the National Computing Facilities (NCF project SH-060-12). Finally, we thank Leo Kroon (Wageningen University) and two anonymous reviewers for their suggestions in improving the manuscript.

References

Bartok J, Bott A, Gera M (2012) Fog prediction for road traffic safety in a coastal desert region. Boundary-Layer Meteorol 145:485–506

Beljaars ACM, Bosveld FC (1997) Cabauw data for the validation of land surface parametrization schemes. J Clim 10:1172–1193

Bergot T, Guedalia D (1994) Numerical forecasting of radiation fog. Part I: numerical model and sensitivity tests. Mon Weather Rev 122:1218–1230

Bergot T, Carrer D, Noilhan J, Bougeault P (2005) Improved site-specific numerical prediction of fog and low clouds: A feasibility study. Weather Forecast 20:627–646

Bergot T, Terradellas T, Cuxart J, Mira T, Liechti O, Müller M, Nielsen NW (2007) Intercomparison of single-column numerical models for the prediction of radiation fog. J Appl Meteorol Climatol 46:504–521

Bosveld F, Baas P, Steeneveld GJ, Holtslag A, Angevine W, Bazile E, de Bruijn E, Deacu D, Edwards J, Ek M, Larson V, Pleim J, Raschendorfer M, Svensson G (2014) The third GABLS intercomparison case for

evaluation studies of boundary-layer models: part B: results and process understanding. Boundary-Layer Meteorol 152:157–187
Bott A, Trautmann T (2002) PAFOG—a new efficient forecast model of radiation fog and low-level stratiform clouds. Atmos Res 64:191–203
Bott A, Sievers U, Zdunkowski W (1990) A Radiation Fog Model with a detailed treatment of the interaction between radiative transfer and fog microphysics. J Atmos Sci 47:2153–2166
Brown R, Roach WT (1976) The physics of radiation fog: II-A numerical study. Q J R Meteorol Soc 102:335–354
Chen F, Dudhia J (2001) Coupling an advanced land surface-hydrology model with the Penn State-NCAR MM5 modeling system. Part I: model implementation and sensitivity. Mon Weather Rev 129:569–585
Chen F et al (2007) Description and evaluation of the characteristics of the NCAR high-resolution land data assimilation system. J Appl Meteorol Climatol 46:694–713
Cuxart J, Jiménez MA (2011) Deep radiation fog in a wide closed valley: study by numerical modeling and remote sensing. Pure Appl Geophys 169:911–926
Cuxart J, Bougeault P, Redelsberger JL (2000) A turbulence scheme allowing for mesoscale and large-eddy simulations. Q J R Meteorol Soc 126:1–30
de Rooy WC, Siebesma AP (2008) A simple parametrization for detrainment in shallow cumulus. Mon Weather Rev 136:560–576
de Rooy WC, Siebesma AP (2010) Analytical expressions for entrainment and detrainment in cumulus convection. Q J R Meteorol Soc 136:1216–1227
Dudhia J (1989) Numerical study of convection observed during the winter monsoon experiment using a mesoscale two-dimensional model. J Atmos Sci 46:3077–3107
Duynkerke PG (1991) Radiation fog: a comparison of model simulation with detailed observations. Mon Weather Rev 119:324–341
Duynkerke PG (1999) Turbulence, radiation and fog in Dutch stable boundary layers. Boundary-Layer Meteorol 90:447–477
Edwards JM (2009) Radiative processes in the stable boundary layer: part I. Radiative aspects. Boundary-Layer Meteorol 131:105–126
Foken T (2008) The energy balance closure problem: an overview. Ecol Appl 18:1351–1367
Fu G, Guo J, Xie SP, Duan Y, Zhang M (2006) Analysis and high-resolution modeling of a dense fog event over the Yellow Sea. Atmos Res 81:293–303
Fu G, Li P, Crompton JG, Guo J, Gao S, Zhang S (2010) An observational and modeling study of a sea fog event over the Yellow Sea on 1 August 2003. Meteorol Atmos Phys 107:149–159
Gultepe I, Tardif R, Michaelides SC, Cermak J, Bott A, Bendix J, Muller M, Pagowski M, Hansen B, Ellrod G, Jacobs W, Toth G, Cober SG (2007) Fog research: a review of past achievements and future perspectives. Pure Appl Geophys 164:1121–1159
Ha KJ, Mahrt L (2003) Radiative and turbulent fluxes in the nocturnal boundary layer. Tellus 55A:317–327
Holtslag AAM, Svensson G, Baas P, Basu S, Beare B, Beljaars ACM, Bosveld FC, Cuxart J, Lindvall J, Steeneveld GJ, Tjernström M (2013) Stable atmospheric boundary layers and diurnal cycles—challenges for weather and climate models. Bull Am Meteorol Soc 94:1691–1706
Kleczek MA, Steeneveld GJ, Holtslag AAM (2014) Evaluation of the weather research and forecasting mesoscale model for GABLS3: impact of boundary-layer schemes, boundary conditions and spin-up. Boundary-Layer Meteorol 152:213–243
Leduc M, Laprise R (2009) Regional climate model sensitivity to domain size. Clim Dyn 32:833–854
Leduc M, Laprise R, Moretti-Poisson M, Morin JP (2011) Sensitivity to domain size of mid-latitude summer simulations with a regional climate model. Clim Dyn 37:343–356
Le Moigne P (2012) Surfex scientific documentation, 237 pp. http://www.cnrm.meteo.fr/surfex/IMG/pdf/surfex_scidoc_v2.pdf
Masson V, Champeaux JL, Chauvin F, Meriguet C, Lacaze R (2003) A global database of land surface parameters at 1-km resolution in meteorological and climate models. J Clim 16:1261–1282
Mlawer EJ, Taubman SJ, Brown PD, Iacono MJ, Clough SA (1997) Radiative transfer for inhomogeneous atmospheres: RRTM, a validated correlated-k model for the longwave. J Geophys Res 102:16663–16682
Müller MD, Masbou M, Bott A (2010) Three-dimensional fog forecasting in complex terrain. Q J R Meteorol Soc 136:2189–2202
Nakanishi M, Niino H (2006) An improved Mellor–Yamada level-3 model: its numerical stability and application to a regional prediction of advection fog. Boundary-Layer Meteorol 119:397–407
Pinty JP, Jabouille P (1998) A mixed-phase cloud parametrization for use in mesoscale nonhydrostatic model: simulations of a squall line and of orographic precipitations. Preprints Conference on cloud physics. American Meteorological Society, Everett, pp 217–220

Rémy S, Bergot T (2009) Assesing the impact of observations on a local numerical fog prediction system. Q J R Meteorol Soc 135:1248–1265
Román-Cascón C, Yagüe C, Sastre M, Maqueda M, Salamanca F, Viana S (2012) Observations and WRF simulations of fog events at the Spanish Northern Plateau. Adv Sci Res 8:11–18
Savijärvi H (2006) Radiative and turbulent heating rates in the clear-air boundary layer. Q J R Meteorol Soc 132:147–161
Siebesma AP, Soares PMM, Teixeira J (2007) A combined Eddy Diffusivity Mass Flux approach for the convective boundary layer. J Atmos Sci 64:1230–1248
Skamarock WC, Klemp JB, Dudhia J, Gill DO, Barker DM, Duda MG, Huang XY, Wang W, Powers WG (2008) A description of the advanced research WRF, Version 3. NCAR Technical Note, Boulder
Steeneveld GJ, Wokke MJJ, Groot Zwaaftink CD, Pijlman S, Heusinkveld BG, Jacobs AFG, Holtslag AAM (2010) Observations of the radiation divergence in the surface layer and its implication for its parametrization in numerical weather prediction models. J Geophys Res 115:D06107
Steeneveld GJ, Tolk LF, Moene AF, Hartogensis OK, Peters W, Holtslag AAM (2011) Confronting the WRF and RAMS mesoscale models with innovative observations in the Netherlands—evaluating the boundary-layer heat budget. J Geophys Res 116:D23114
Stolaki S, Pytharoulis I, Karacostas T (2011) A study of fog characteristics using a coupled WRF-COBEL Model over Thessaloniki Airport, Greece. Pure Appl Geophys 169:961–981
Syed FS, Körnich H, Tjernström M (2012) On the fog variability over south Asia. Clim Dyn 39:2993–3005
Tanaka H, Honma S, Nishi M, Igarashi T, Teramoto S, Nishio F, Abe S (1998) Acid fog and hospital visits for asthma: an epidemiological study. Eur Respir J 11:1301–1306
Teixeira J (1999) Simulation of fog with the ECMWF prognostic cloud scheme. Q J R Meteorol Soc 125:529–552
Thoma C, Schneider W, Masbou M, Bott A (2012) Integration of local observations into the one dimensional fog model PAFOG. Pure Appl Geophys 169:881–893
Tudor M (2010) Impact of horizontal diffusion, radiation and cloudiness parametrization schemes on fog forecasting in valleys. Meteorol Atmos Phys 108:57–70
Undén P et al. (2002) HIRLAM-5 scientific documentation. HIRLAM-5 Project, SMHI, Norrkoping, Sweden, 146 pp. http://www.hirlam.org/open/publications/SciDoc_Dec2002.pdf
Van der Velde IR, Steeneveld GJ, Holtslag AAM (2010) Modeling and forecasting the onset and duration of severe radiation fog under frost conditions. Mon Weather Rev 138:4237–4253
Warner TT, Peterson RA, Treadon RE (1997) A tutorial on lateral boundary conditions as a basic and potentially serious limitation to regional numerical weather prediction. Bull Am Meteorol Soc 78:2599–2617
Wild M, Ohmura A, Gilgen H, Morcrette JJ, Slingo A (2001) Evaluation of downward longwave radiation in general circulation models. J Clim 14:3227–3239
Zhou B, Du J, Gultepe I, Dimego G (2011) Forecast of low visibility and fog from NCEP: current status and efforts. Pure Appl Geophys 169:895–909